Enhancing Surface Sensitivity of Nanostructure-Based Aluminum Sensors Using Capped Dielectric Layers

Kuang-Li Lee,*,[†] Po-Cheng Tsai,[‡] Meng-Lin You,[†] Ming-Yang Pan,[†] Xu Shi,[§] Kosei Ueno,[§] Hiroaki Misawa,[§,∥] and Pei-Kuen Wei*,[†,‡,⊥]

[†]Research Center for Applied Sciences, Academia Sinica, 128, Section 2, Academia Road, Nangkang, Taipei 11529, Taiwan
[‡]Institute of Optoelectronic Sciences, National Taiwan Ocean University, Keelung 20224, Taiwan
[§]Research Institute for Electronic Science, Hokkaido University, Hokkaido 060-0808, Japan
[∥]Department of Applied Chemistry, National Chiao Tung University, Hsinchu 20010, Taiwan
[⊥]Institute of Biophotonics, National Yang-Ming University, Taipei 11221, Taiwan

ABSTRACT: The studies of nanostructure-based aluminum sensors have attracted huge attention because aluminum is a more cost-effective plasmonic material. However, the intrinsic properties of the aluminum metal, having a large imaginary part of the dielectric function and a longer electromagnetic field decay length and problems of poor long-term chemical stability, limit the surface-sensing capability and applicability of nanostructures. We propose the combination of capped aluminum nanoslits and a thin-capped dielectric layer to overcome these limitations. We show that the dielectric layer can positively enhance the wavelength sensitivities of the Wood's anomaly-dominant resonance and asymmetric Fano resonance in capped aluminum nanoslits. The maximum improvement can be reached by a factor of 3.5. Besides, there is an optimal layer thickness for the surface sensitivity because of the trade-off relationship between the refractive index sensitivity and decay length. We attribute the enhanced surface sensitivity to a reduced evanescent length, which is confirmed by the finite difference time-domain calculations. The protein−protein interaction experiments verify the high-surface sensitivity of the structures, and a limit of quantification (LOQ) of 1 pg/mL anti-bovine serum albumin is achieved. Such low-cost, highly sensitive aluminum-based nanostructures can benefit various sensing applications.
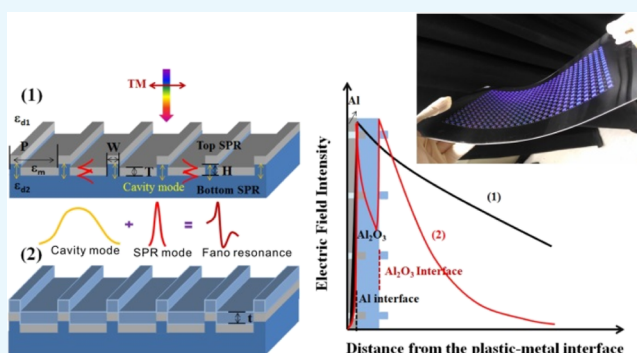
1. INTRODUCTION

Nanostructure-based surface plasmon resonance (SPR) sensing has the features of sensitive, real-time, and label-free detection and is applied to many applications, such as environmental monitoring, medical diagnostics, and food safety.[1−4] Compared to the commercial prism-based SPR sensors, nanostructure-based SPR sensors provide a simple way for SPR excitation and have some benefits, including small detection volume, simple measurement, and ease of multiple detections.[5−11] Noble metals such as Au and Ag are commonly used for the majority of the plasmonic sensors because these materials have low optical losses in the visible and near-infrared ranges. Recently, the studies of nanostructure-based aluminum sensors have attracted a lot of attention because aluminum is a cost-effective plasmonic material and useful for short-wavelength surface plasmons. Various aluminum-based nanostructures such as nanoconcave arrays,[12] nanoholes,[13−15] triangular nanoparticles,[16] and capped nanoslits[17] have been proposed. To use the Al material for sensing, the problems of poor long-term chemical stability have to be solved. These issues can be addressed by depositing a passivation dielectric film or using a passivation treatment based on oxygen plasma to produce an oxide-protecting layer.[18] However, the large imaginary part of the dielectric function for aluminum results in a broad resonance response and a longer electromagnetic field decay length, which limits its surface-sensing capability. Therefore, improving surface sensitivities of aluminum-based nanostructures is an important issue.

To evaluate the surface-sensing capabilities of different nanostructures, the effective refractive index (n_{eff}) due to the immobilized biolayer is approximated as follows[19]

$$n_{eff} = n_s \exp(-2d/l_d) + n_a[1 - \exp(-2d/l_d)] \qquad (1)$$

where d is the biolayer thickness, n_s is the bulk solution refractive index, n_a is the adsorbate monolayer refractive index, and l_d is the length of the surface evanescent field. The wavelength shift ($\Delta\lambda$) caused by the biolayer can be expressed as[19]
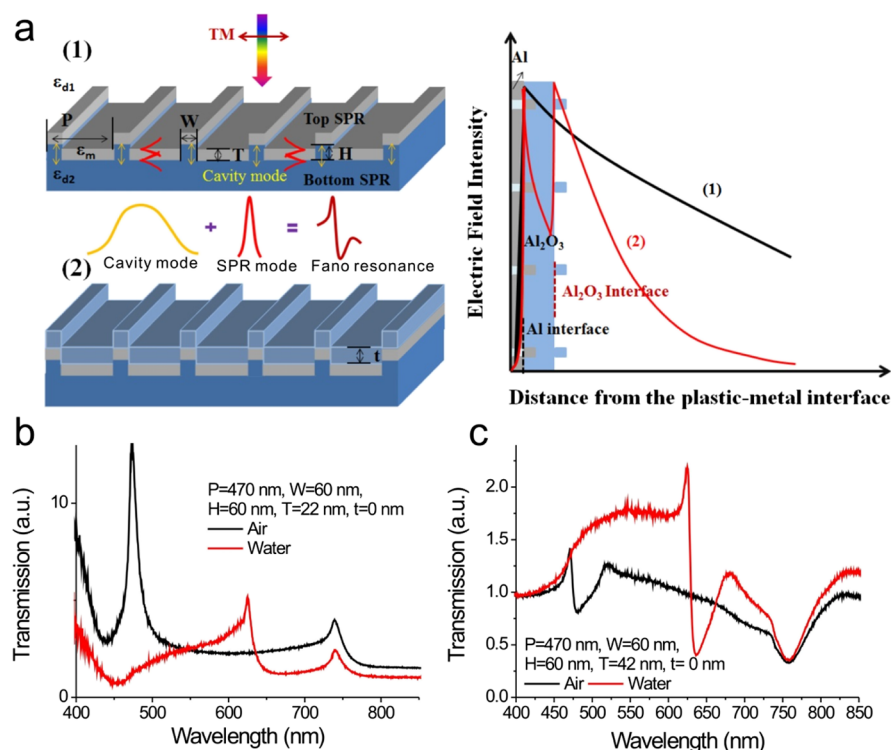
Figure 1. Optical properties of aluminum-capped nanoslits and alumina/aluminum-capped nanoslits. (a) Electric-field distributions in aluminum-capped nanoslits and alumina/aluminum-capped nanoslits. The left panel shows a schematic configuration depicting the geometrical parameters of the aluminum-capped nanoslits (1) and alumina/aluminum-capped nanoslits (2), the direction of the TM-polarized incident light and the Fano resonance. The right panel shows a schematic diagram depicting the electric-field distributions at metal and alumina interfaces for aluminum-capped nanoslits and alumina/aluminum-capped nanoslits. The thin dielectric layer changes the resonance-field distribution and reduces the decay length. (b,c) Measured transmission spectra of the 470 nm period capped aluminum nanoslits in air and water for normally incident TM-polarized light. We chose H = 60 nm, T = 22 (b) and 42 nm (c), W = 60 nm, P = 470 nm, and t = 0 nm for the structures.

$$\Delta\lambda = S_\lambda(n_{eff} - n_s) = S_\lambda(n_a - n_s)[1 - \exp(-2d/l_d)] \quad (2)$$

where S_λ is the bulk (refractive index) sensitivity, defined as $\Delta\lambda/\Delta n_s$. The surface sensitivity is related to the bulk sensitivity, refractive index difference between the adsorbate monolayer and the surrounding environment, and evanescent decay length. To improve the sensing capabilities of SPR sensors, many approaches, such as the spectral integration analysis,[20−23] thermal-annealing nanoimprint method,[24−27] Fano coupling,[28−32] narrowing resonance bandwidth with oblique angle incidence,[33] magneto-optic SPR sensors,[34−37] and nearly guided-wave SPR sensors,[38] were proposed. The spectral integration analysis considers wavelength shifts and intensity changes near the resonances, which is able to improve the signal-to-noise ratio of the system and enhance the sensing capability.[21−24] To increase the resonant slope, Fano resonances in nanostructures are proposed. The Fano resonance exhibits a distinctly asymmetric shape, which arises from the spectral overlap between a narrow discrete resonance and a broad resonance.[30] The Fano resonances have been extensively studied in various nanoparticles,[39] plasmonic nanostructures,[9,31] and metamaterials.[40] To reduce the evanescent decay length, a nearly guided wave SPR sensor, a thin silicon top layer on the SPR sensor, is proposed. This structure enables the surface plasmons to spread along the dielectric layer and increases the interaction volume, which improves the sensitivity by a factor of 4.[41]

In this study, we proposed the combination of Fano resonances in capped nanoslits and a thin capped dielectric layer to improve the surface sensitivities of aluminum-based nanostructures (see Figure 1a). The thin dielectric layer changes the resonance field distribution, reduces the decay length, increases the interaction volume, and improves the surface sensitivity. We utilized hot embossing nanoimprint lithography, thermal evaporation, and atomic layer deposition (ALD) to fabricate low-cost, large-area, and highly sensitive alumina-/aluminum-capped nanoslit arrays on plastic films. The optical properties of these aluminum nanostructures with different resonance profiles and dielectric layer thicknesses were studied; their surface sensitivities were compared using wavelength interrogation. Moreover, the sensing capabilities of the proposed nanostructures were verified by measuring the protein−protein interactions between bovine serum albumin (BSA) and anti-BSA. We showed that the capped dielectric layer can enhance the surface sensitivities of the Wood's anomaly-dominant resonance and asymmetric Fano resonance in capped aluminum nanoslits. The maximum improvement can be reached by a factor of 3.5. Although the dielectric layer reduced the bulk refractive index sensitivity, the surface sensitivity was improved because of the reduced decay length, which was confirmed by the finite-difference time-domain (FDTD) calculations. Besides, there was an optimal dielectric layer thickness for the surface sensitivity because of the trade-off relationship between the refractive index sensitivity and decay length. The protein−protein interaction experiments verified the high sensitivity of the alumina-/aluminum-capped nanostructures, and a limit of quantification (LOQ) of 1 pg/mL anti-BSA was achieved.
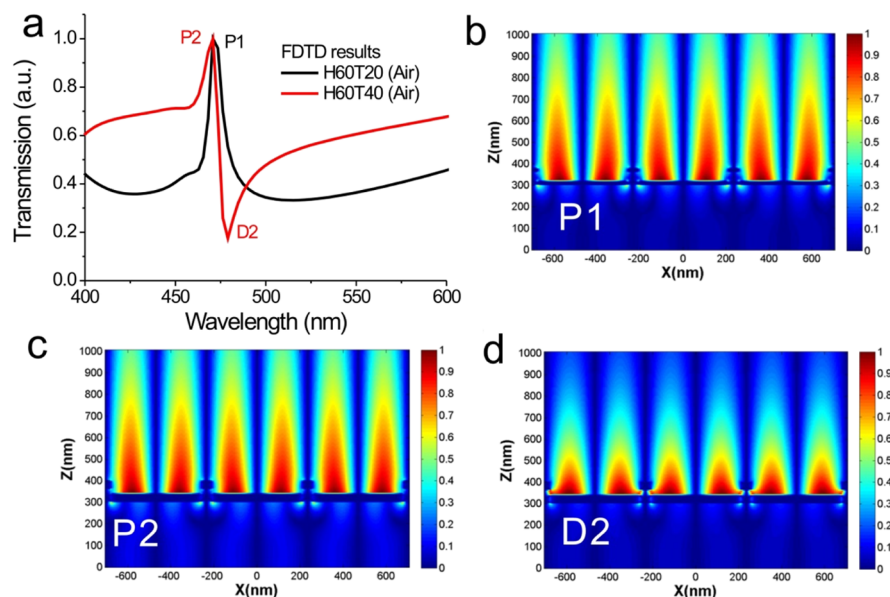
Figure 2. Comparison of Wood's anomaly-dominant and Fano resonances in capped aluminum nanoslits using FDTD calculations. (a) Calculated transmission spectra of the 470 nm period capped aluminum nanoslits with different structure parameters. The structure parameters were P = 470 nm, H = 60 nm, T = 20−40 nm, W = 60 nm, and t = 0 nm. (b−d) Resonance-field (E_z) distribution for the resonance peaks P1 (b) and P2 (c), and dip D2 (d), respectively. The Fano resonance dip (D2) has a shorter decay length than the Fano resonance peak (P2) or the Wood's peak (P1). The calculated decay lengths were 883, 891, and 338 nm for P1, P2, and D2, respectively.

2. RESULTS AND DISCUSSION

2.1. Optical Properties of the Capped Aluminum Nanoslits.

Figure 1a shows a schematic configuration depicting the geometrical parameters of the capped aluminum nanoslits and the direction of the transverse magnetic (TM)-polarized incident light. Figure 1b,c shows the measured transmission spectra of the 470 nm period capped aluminum nanoslits with different heights of metal films in air and water for normally incident TM-polarized light. We chose H (*slit height*) = 60 nm, T (*Al thickness*) = 22 and 42 nm, W (*slit width*) = 60 nm, P (*period*) = 470 nm, and t (Al$_2$O$_3$ *film thickness*) = 0 nm for the structures. For T = 42 nm nanostructure, there are transmission peaks and dips in the spectrum because of the couplings of cavity resonances in nanoslits and surface waves on both sides of the periodic aluminum surface (the aluminum/medium and aluminum/substrate interfaces). The gap plasmons transmit through the nanoslits and the capping layer, leading to a broadband transmission within a cavity spectrum. The resonance condition can be estimated using a Fabry−Perot cavity.[42] The resonance wavelength is related to the gap width and cavity length. The cavity mode is coupled to the surface waves from the edges of the top and bottom interfaces and coupled to the Bloch wave surface plasmon polariton (BW-SPP). The BW-SPP occurs when the Bragg condition is satisfied. The Bragg condition for one-dimensional arrays can be described by[1]

$$\lambda_{\text{SPR}}(n, i) = \frac{P}{i}\left\{\text{Re}\left[\left(\frac{\varepsilon_{\text{m}}n^2}{\varepsilon_{\text{m}} + n^2}\right)^{1/2}\right]\right\} \tag{3}$$

where i is the resonance order, P is the period of the nanostructure, and n is environmental refractive index. The interaction between cavity resonances in nanoslits (a continuum state) and BW-SPPs (a discrete resonance state) creates a Fano resonance profile consisting of a minimum (dip) and an adjacent maximum (peak).[29,43,44] It generates a sharp

resonance profile. In the case of capped nanoslit arrays with a 470 nm period and a 42 nm thick metal film, extremely sharp Fano resonances were observed. The resonance dip wavelengths of Fano resonances at the air/aluminum, water/aluminum, and substrate/aluminum interfaces were 481, 636, and 757 nm, respectively. On the other hand, for T = 22 nm thick nanostructure, the metal film was too thin to form a continuous film on 60 nm high nanoslits. The direct transmission through the metal film and Wood's anomaly contributes to the transmission spectrum. The redistribution of diffracted photons results in the Wood's anomaly, and a transmission peak appears under the condition

$$\lambda_{\text{Wood}}(n, i) = \frac{P}{i}n \tag{4}$$

The measured resonance peak wavelengths at the air/aluminum, water/aluminum, and substrate/aluminum interfaces were 473, 625, and 739 nm, respectively. These values are quite consistent with the theoretical predictions, that is, 470 (air, n = 1), 625.1 (water, n = 1.33), and 737.9 (substrate, n = 1.58).

We further utilized FDTD (FullWAVE 4.0, RSoft) simulations to verify the measured spectra and the decay lengths for the resonance at peak and dip wavelengths. Figure 2a shows the calculated transmission spectra of the 470 nm period capped aluminum nanoslits with different structure parameters for normally incident TM-polarized light. The structure parameters were P = 470 nm, H = 60 nm, T = 20−40 nm, W = 60 nm, and t = 0 nm. The resonances with different resonance profiles were observed in the calculated spectra. These resonance profiles match quite well with the measured results, as shown in Figure 1b,c. Figure 2b−d shows the resonance field (E_z) distributions for the resonance peaks (P1 and P2) and dip (D2), respectively. Obviously, the Fano resonance dip (D2) has a shorter decay length than the Fano resonance peak (P2) or the Wood's peak (P1). The calculated
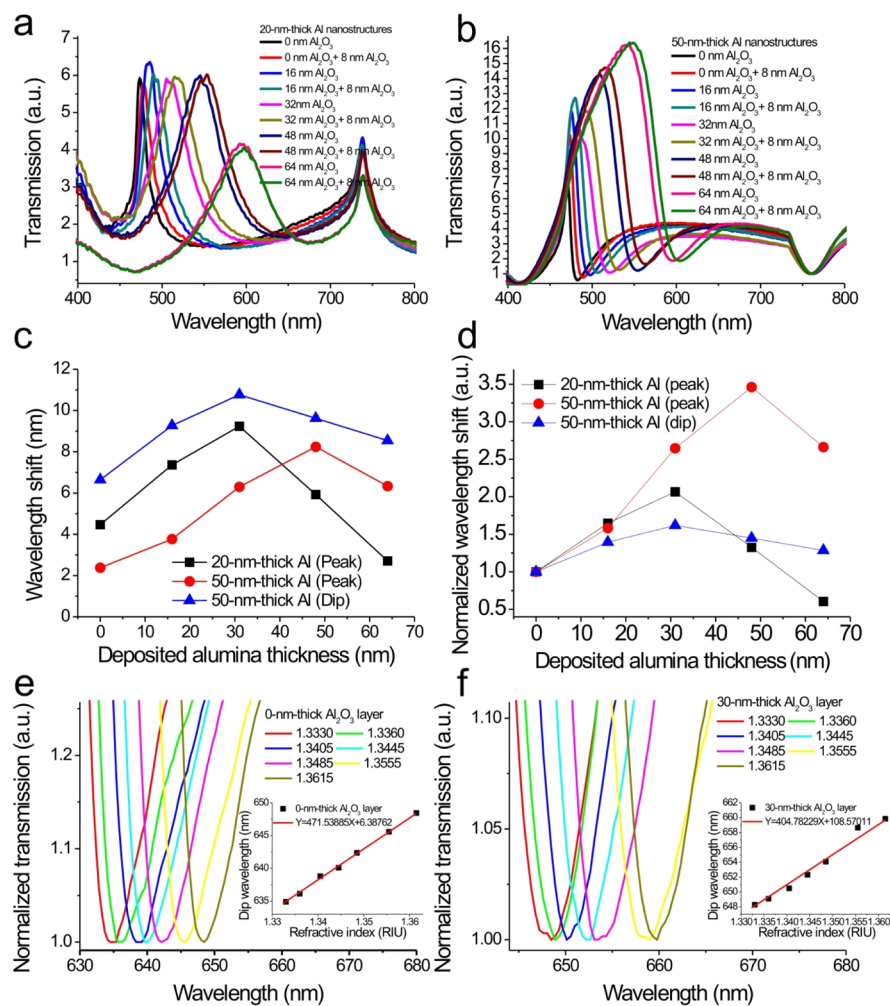
Figure 3. Surface and refractive index sensitivity tests for alumina/aluminum-capped nanoslits using wavelength interrogation. The transmission spectra of capped aluminum nanoslits with metal thicknesses of 20 nm (a) and 50 nm (b) for different deposited Al_2O_3 film thicknesses from 0 to 64 nm. (c) Wavelength shift caused by an 8 nm thick Al_2O_3 film against the passivation film thickness for different aluminum nanostructures. (d) Normalized wavelength shift against the dielectric layer thickness for different aluminum nanostructures. The peak or dip wavelength shift of bare aluminum nanostructures was chosen as a reference. (e,f) Transmission spectra of the capped aluminum nanoslits without dielectric layers (e) and with a 32 nm thick Al_2O_3 film (f) in various water/glycerin mixtures. The slopes of the fitting curves show that the bulk sensitivities were 471 and 404 nm/RIU.

decay lengths were 883, 891, and 338 nm for P1, P2, and D2, respectively. These results indicate that the Fano resonance dip has a higher surface sensitivity than other resonance peaks. However, these peaks show sharper resonance profiles than the Fano dip as shown in the experimental results. The bandwidth of the peak resonance is 3.4 times narrower than that of the Fano dip, as shown in Figure 1c. The resonant peak has a better resolution for wavelength and intensity measurement because of its sharp slope. We found that the use of a thin-capped dielectric layer can greatly reduce the decay lengths and enhance the surface sensitivities of these resonance peaks.

2.2. Surface and Refractive Index Sensitivity Tests for Alumina-/Aluminum-Capped Nanoslits. We study the effect of the dielectric layer on the surface sensitivities of the nanostructures by depositing different thicknesses (t) of Al_2O_3 films. We prepared some alumina-/aluminum-capped nanoslits and recorded their transmission spectra. The thickness of Al_2O_3 dielectric films ranged 0−64 nm. After an 8 nm thick Al_2O_3 film was deposited on the structures, the spectra were recorded again. Figure 3a,b shows the spectrum of nanostructures with metal thicknesses of 20 nm (Wood's anomaly-dominant) and

50 nm (Fano resonance-dominant) for different Al_2O_3 film thicknesses, respectively. The resonance peaks and the dip were red-shifted when Al_2O_3 film was deposited on the structures. The measured wavelength shifts for the resonance peaks and dip are shown in Figure 3c. Without dielectric layers, the shifts were 4.4 and 2.3 and 6.6 nm for $T = 20$ nm and $T = 50$ nm nanostructures, respectively. The resonance dip has a higher sensitivity than the resonance peaks because of its shorter decay length. The spectral shifts gradually increased and reached their maximum when the alumina layers reached about 32−48 nm. The maximal shifts were 9.2 and 10.7 nm for $T = 20$ nm and $T = 50$ nm thick nanostructures, respectively. When the dielectric layers further increased, the shifts decreased. Compared to the sensor without the dielectric layer, the nanostructures with dielectric layers had higher sensitivities. The spectral shift was improved by a factor of 2 for 20 nm thick nanostructures. For 50 nm thick sensors, the shifts increased by factors of 3.5 and 1.6 for the resonance peak and dip, respectively (see Figure 3d). We estimated the surface sensitivities of the 50 nm thick nanostructures with 30 nm thick dielectric layers by calculating the wavelength shifts caused by the 30 nm thick Al_2O_3 films.
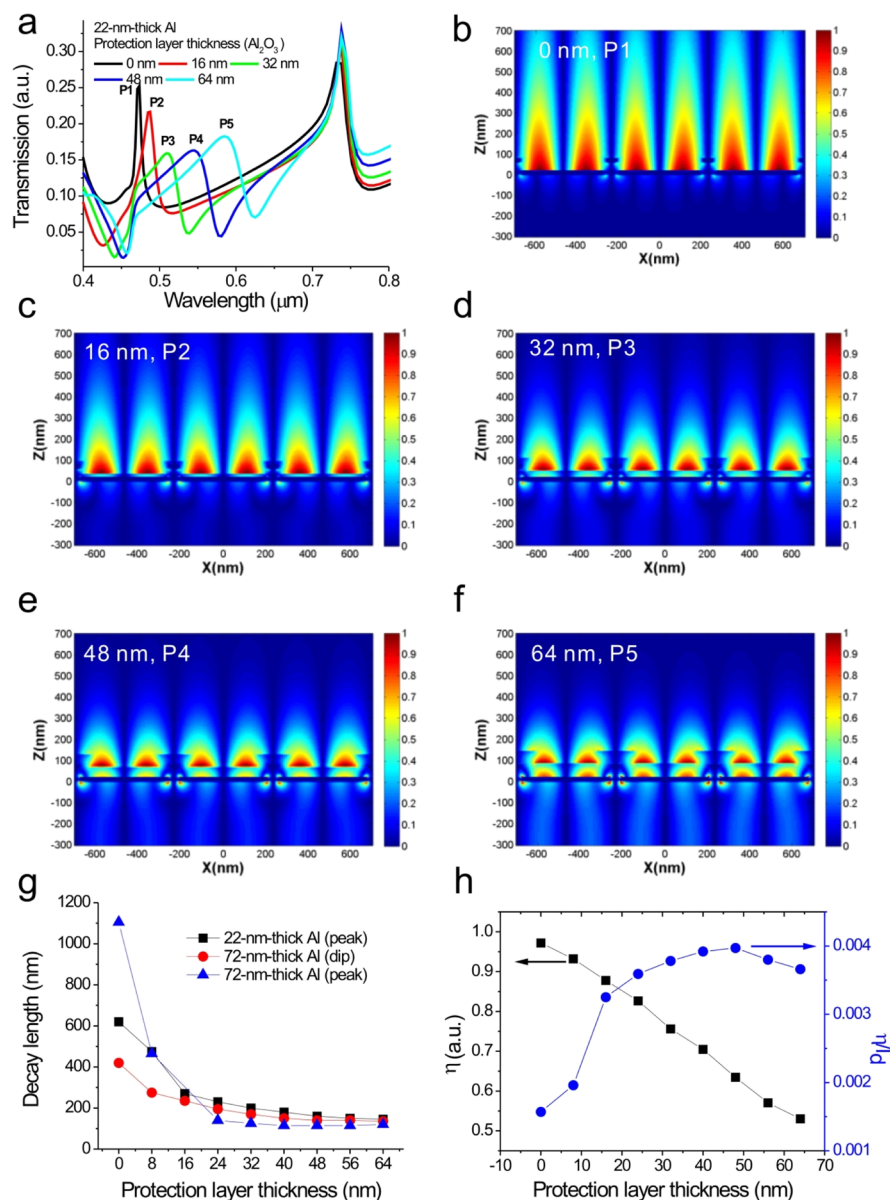
Figure 4. Calculated transmission spectra and resonance-field distributions of alumina/aluminum-capped nanoslits using FDTD calculations. (a) Calculated transmission spectra of the capped aluminum nanoslits with different thicknesses of alumina layers for normally incident TM-polarized light. The structure parameters were P = 470 nm, H = 60 nm, T = 22 nm, W = 60 nm, and t = 0−64 nm. (b−f) Resonance field (E_z) distributions for the resonance peaks (P1−P5). (g) Calculated decay lengths at peak and dip wavelengths for the Wood's anomaly-dominant resonance (T = 22 nm) and Fano resonance in capped nanoslits (T = 72 nm). (h) Overlapping degree (η) between the field intensity in the sensing volume and all-field intensity and ratio (η/l_d) as a function of the alumina thickness.

They ranged from 1.6 to 1.8 nm/nm. With 0.1 nm wavelength resolution, the capped aluminum nanoslits can detect about 0.05 nm thick biolayer films on the surface.

According to eq 2, when the film thickness (d), the bulk solution refractive index (n_s), and the refractive index of the thin film (n_a) are chosen, the spectral shift is determined by the bulk sensitivity (S_λ) and decay length (l_d). To confirm the effect of the dielectric layer on the refractive index sensitivity, we measured the refractive index sensitivities of 50 nm thick-capped nanoslits without and with a 30 nm thick alumina layer, as shown in Figure 3e,f. The results show that the bulk sensitivities were 471 and 404 nm/RIU, respectively. This indicates that the dielectric layer not only reduces the decay length but also decreases the bulk sensitivity. There is a trade-off between S_λ and l_d. The optimal condition for dielectric-

coating thickness occurs at t = 30−50 nm. In the optimal case, the surface wavelength sensitivity for the alumina-/aluminum-capped nanostructures was increased up to three times. We attributed the improved wavelength sensitivity to the reduced decay length caused by the capped dielectric layer. When the dielectric layer is deposited on the metal surface of the nanostructures, the optical field is redistributed, resulting in the reduced decay length.

2.3. Transmission Spectra and Resonance Field Distributions of the Alumina-/Aluminum-Capped Nanoslits Using FDTD Calculations. To confirm and explain the observed results, we further utilized FDTD calculations to calculate the transmission spectra and resonance field distributions of the capped nanoslits. Figure 4a shows the calculated transmission spectra of the 470 nm period, 22 nm
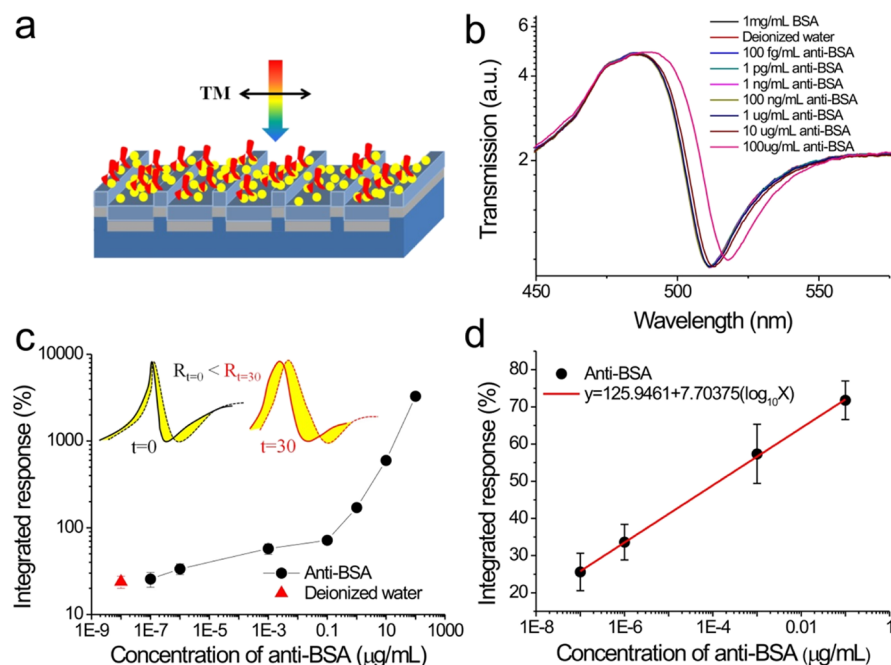
Figure 5. Surface sensitivity tests of 470 nm period alumina/aluminum-capped nanoslits by measuring the interactions between BSA and anti-BSA. (a) Schematic cartoon showing the measurement of the interactions between BSA and anti-BSA using alumina/aluminum-capped nanoslits. (b) Measured transmission spectra in 1 mg/mL BSA, deionized water, and different concentrations of anti-BSA solutions from 100 fg/mL to 100 μg/mL. (c) Integrated responses caused by deionized water and different concentrations of anti-BSA solutions. The intensity spectrum of the BSA solution was set as a reference. The inset shows the integrated responses for capped nanoslits with and without a dielectric film. (d) Integrated response as a function of the logarithm of the concentration of the anti-BSA solution.

thick capped aluminum nanoslits with various thicknesses of Al_2O_3 films for normally incident TM-polarized light. The structure parameters were $P = 470$ nm, $H = 60$ nm, $T = 22$ nm, and $W = 60$ nm. The oxide layer (t) ranged from 0 to 64 nm. The Wood's anomaly-dominant resonances were observed in the calculated spectra. These resonance profiles agree quite well with the measured results, as shown in Figure 3a. The resonance was red-shifted and became broader with the increase of the deposited oxide layer. Figure 4b−f shows the resonance field (E_z) distributions at peak wavelengths for different Al_2O_3 layers. Obviously, resonance field distributions changed and were gradually confined to the oxide layer. The average decay length, calculated from the resonance field (E_z) distributions, was 620 nm for the structure without the dielectric layer. It decreased to 145 nm and reduced by a factor of 4.2 when the oxide layer increased to 64 nm, as shown in Figure 4g. A similar tendency was observed for the asymmetric Fano resonance in capped aluminum nanoslits. The decay lengths for the peak and dip wavelengths were 1105 and 420 nm, respectively. When the thick oxide layer was deposited on the metal surface, the field distribution of the Fano mode was affected and the decay lengths reduced to 120 and 135 nm, respectively. They reduced by factors of 9.2 and 3.1. It was noted that the surface wavelength sensitivity is determined by the bulk sensitivity (S_λ) and decay length (l_d). The effect of S_λ related to the dielectric-coating thickness should also be considered. The S_λ can be evaluated by $S_\lambda(t) = \eta S_\lambda(0)$, where $S_\lambda(0)$ is the bulk (wavelength) sensitivity when t is zero and η is the overlapping degree between the field intensity in the sensing volume (air) and all volume, that is,

$$\eta = \frac{\int_t^\infty E_z^2 \, dz}{\int_{-\infty}^\infty E_z^2 \, dz} \tag{5}$$

With the increase of the dielectric layer thickness, more field intensity was confined to the oxide layer and the η decreased, resulting in reduced bulk sensitivities, as shown in Figure 4h. Therefore, the bulk sensitivity is oxide-thickness-dependent. According to eq 2, when the biolayer thickness is very small, the spectral shift is proportional to the bulk sensitivity and decay length, that is, $\Delta\lambda \propto S_\lambda(t)/l_d = S_\lambda(0)(\eta/l_d)$. Both the η and decay length were dependent on the dielectric-coating thickness. The coating layer shortened the decay length and reduced the bulk sensitivity; it caused different decrease rates for both parameters. The competition between these two parameters results in the optimal condition for the surface sensitivity, as shown in Figure 4h. The optimal thickness is about 50 nm, which agrees quite well with the measured results (see Figure 3d). Therefore, the improved surface sensitivity for structures with dielectric layers is attributed to the reduced decay length. Besides, owing to the decrease of bulk sensitivity, there is an optimal condition for the coating-layer thickness.

2.4. Surface Sensitivity Tests of 470 nm Period Alumina-/Aluminum-Capped Nanoslits by Measuring the Interactions between BSA and Anti-BSA. To verify the surface sensitivity of the 470 nm period capped aluminum nanoslits with a 32 nm thick Al_2O_3 layer, we further immobilized BSA proteins on the chip and detected different concentrations of the anti-BSA solutions, as shown in Figure 5a. The measured transmission spectra in 1 mg/mL BSA, deionized water, and different concentrations of anti-BSA solutions from 100 fg/mL to 100 μg/mL are shown in Figure 5b. The Fano resonances were red-shifted with the increase of
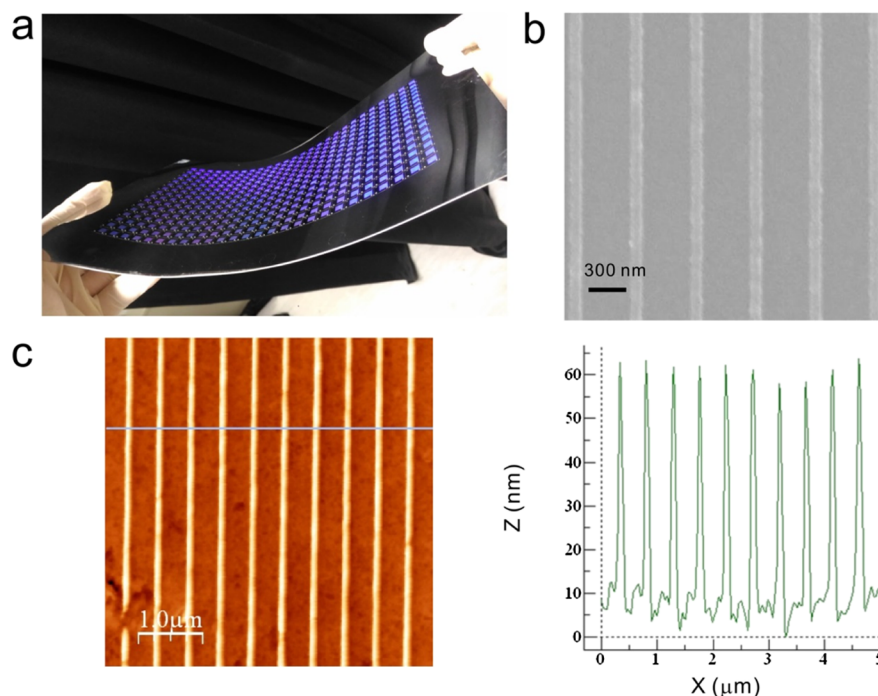
Figure 6. Fabrication of capped aluminum nanoslits using hot embossing nanoimprint lithography and thermal evaporation. (a) Optical image of the capped aluminum nanoslit arrays. There are 416 arrays on an A4-sized PC film. The area of each periodic nanostructure is 5×5 mm^2. (b) SEM image of the capped aluminum nanoslits. (c) AFM image (left panel) and cross-sectional profile (right panel) of the capped aluminum nanoslits. The ridge height is 60 nm.

the concentration of anti-BSA solutions. In this experiment, the minispectrometer has a spectral resolution of 0.4 nm, which limits the sensing capability of the structures. To enhance the limit of detection, the spectral data can be analyzed using the spectral integration method.[20−23] The advantage of the combination of proposed structures and the spectral integration method is illustrated in the inset of Figure 5c. As the alumina-/aluminum-capped nanoslits are able to increase the peak and dip wavelength shifts, the summation of the intensity changes $(R_{t=30})$, that is, the spectral integration response, for the proposed structure is larger than that for the nanostructures without a dielectric film $(R_{t=0})$. Therefore, the sensing capability was further improved using the spectral integration method. The response (R) for the spectral integration method is defined by the absolute value of the difference of the normalized intensity spectra

$$R(n) = \sum_{\lambda_1}^{\lambda_2} \left| \frac{I(n, \lambda) - I(n_0, \lambda)}{I(n_0, \lambda)} \right| \times 100\% \tag{6}$$

where the $I(n, \lambda)$ is the transmitted intensity at a wavelength λ under a concentration of the analyte solution (n), n_0 is the reference sample, and λ_1 and λ_2 are the integrated wavelength range. The intensity spectrum of the BSA was set as a reference, and the integrated wavelength range was from $\lambda_1 = 500$ nm to $\lambda_2 = 530$ nm. Figure 5c shows the integrated responses caused by deionized water and different concentrations of anti-BSA solutions. The integrated responses for deionized water, 0.1 pg/mL, 1 pg/mL, 1 ng/mL, 0.1 μg/mL, 1 μg/mL, 10 μg/mL, and 100 μg/mL, were 23.8, 25.5, 33.6, 57.4, 71.8, 170.9, 598.4, and 3280%, respectively. Obviously, the response against the logarithm of the concentration shows two linear correlations, as shown in Figure 5c, and the concentration of the break point is around 0.1 μg/mL. According to eq 2, the sensing response is

related to the refractive index of the biomolecules and exponential growth as the biolayer thickness (d) increases. The equivalent thickness increases with the concentration. Therefore, the response behaves as an exponential curve and can be roughly fitted by two slopes. Figure 5d shows the response against the logarithm of the concentration below 0.1 μg/mL. The calibration curve was described by $y = 7.70375 \cdot (\log_{10}(x)) + 125.9461$ and $R^2 = 0.99961$, and the measured noise was 3.7% (standard deviation of the response). As the response of the deionized water was close to that of 100 fg/mL anti-BSA, we estimated the LOQ of the concentration of anti-BSA to be 1 pg/mL. It is noted that for the anti-BSA detection using a commercial prism-based SPR system, the LOQ is about 0.1 ng/mL. The proposed dielectric-coated capped aluminum nanoslit array can enhance the LOQ by about 2 orders of magnitude.

3. CONCLUSIONS

The intrinsic properties of the aluminum metal, having a large imaginary part of the dielectric function and a longer electromagnetic field decay length and problems of poor long-term chemical stability, limit the surface-sensing capability and applicability of nanostructures. We show that these limitations can be overcome using alumina-/aluminum-capped nanoslit structures. The dielectric layer not only prevents the aluminum from chemical damages but also effectively enhances the wavelength sensitivities of the nanostructure-based aluminum biosensors. For the asymmetric Fano resonance nanostructures, the surface sensitivity was increased by a factor of 3.5 for the resonance peak. The surface sensitivity was improved because of the significant reduction of the decay length. The decay lengths for the Wood's anomaly-dominant resonance, Fano peak, and dip resonances were reduced by factors of 4.2, 9, and 2.9 for a 48 nm dielectric layer. The

protein−protein interaction experiments verified the high sensitivity of the structures, and an LOQ of 1 pg/mL anti-BSA was achieved. As the nanostructures were fabricated on plastic films, they can be directly integrated to the plastic-based microfluidic devices using hot embossing nanoimprint lithography.[45] The sample pretreatment and multiplexed detection can be conducted on a chip, which can contribute to the moving plasmonic biosensors to point-of-care diagnosis.[46] It was noted that other dielectric films such as Si, SiO$_2$, and HfO$_2$ films can also be utilized to improve the surface sensitivity. In this study, the alumina dielectric film is chosen and is suitable for the immobilization of phosphonic acid-ended glycans.[47] The proposed structures have the potential to be applied to a label-free glycan array. Such low-cost, highly sensitive aluminum-based nanostructures can benefit sensing applications.

4. EXPERIMENTAL SECTION

4.1. Nanoimprinting Process for Metallic Nanostructures. The metallic nanostructures were produced on a polycarbonate (PC) plastic substrate using rapid hot embossing nanoimprint lithography and thermal evaporation. First, the metallic templates were made using electron-beam lithography and electroforming. Periodic nanogrooves in a 100 nm thick diluted ZEP-520 resist (ZEP-520, Zeon Corp, Tokyo, Japan) were drawn on a 525 μm thick silicon substrate using an electron-beam writing system (ELS-F125, Elionix, Japan). The width, depth, and period of the periodic nanogrooves were 60, 100, and 470 nm, respectively. The patterns were deposited on a thin gold film and then electroformed with Ni and Co to produce a 250 μm thick metal mold. The template was used to replicate the nanostructures on the 380 μm thick plastic film using homemade hot embossing nanoimprint equipment.[48] With the heating temperature of 185 °C, the replicated plastic nanostructures with a ridge height of 60 nm were made. After depositing the aluminum films with different thicknesses of 22−50 nm on the replicated plastic substrates, the capped aluminum nanoslit arrays were produced. Figure 6a shows the optical image of the 416-capped aluminum nanoslit arrays on an A4-sized PC film. The area of each array is 5 × 5 mm^2. Figure 6b shows the scanning electron microscopy (SEM) image of the capped aluminum nanoslit arrays. The ridge height is 60 nm.

4.2. Atomic Force Microscopy Measurements. Figure 6c shows the atomic force microscopy (AFM) images of the capped aluminum nanoslit arrays, obtained with a Veeco di Innova AFM instrument operating in the tapping mode in air. The cross-sectional profile shows that the ridge height of the nanostructures is 60 nm.

4.3. Optical Setup for Transmission Spectrum Measurement. The 150 W white light was coupled to a fiber cable and a fiber lens for light collimation. The light was incident on a nanostructure array after passing through a linear polarizer, which controls its incident polarization. The transmitted light was then collected by another fiber lens and focused on a fiber cable. The signals were recorded by a fiber-coupled linear charge-coupled device array spectrometer (BWTEK, BTC112E).

4.4. ALD of Aluminum Oxide. The aluminum oxide films with different thicknesses were deposited on capped aluminum nanoslit arrays using an ALD machine (Syskey Technology Co., Ltd.). With the precursors of trimethylaluminum and water, the alumina films were formed under the following deposition

conditions. The substrate temperature was kept at 120 °C, and the chamber working pressure was set to 1.2 × 10^{-1} Torr.

4.5. Refractive Index Sensitivity Tests and Biosensing Experiments. The refractive index sensitivities were checked by measuring different water/glycerin mixtures with refractive indexes ranging from 1.3330 to 1.3615. The BSA (Sigma-Aldrich) and anti-BSA (Sigma-Aldrich) assays in deionized water were conducted using alumina-/aluminum-capped nano-slit arrays. First, to form amino groups on the alumina surface, the nanostructures were dipped in a 10% aminopropyltriethox-ysilane solution for 30 min and washed with ultrapure water. After being purged dry by nitrogen gas, they are baked at 120 °C for 1 h. For amide binding, the modified surface was activated by dipping the nanostructures into a 5% glutaralde-hyde amino reactive bifunctional cross-linker at 25 °C for 30 min. After the surface modification processes, a 100 μL of 1 mg/mL BSA solution was dropped onto the sensing area for 1 h. To remove the unbound BSA proteins, the nanostructures were then washed with ultrapure water and purged dry by nitrogen gas. These procedures were repeated three times to make BSA proteins occupy the sensing surface. Finally, a 100 μL of 100 fg/mL anti-BSA solution was dropped onto the sensing surface for 1 h. After being washed with ultrapure water, the structures were purged dry by nitrogen gas. For detecting different concentrations of anti-BSA solutions from 100 fg/mL to 100 μg/mL, the processes including dropping, washing, and nitrogen-purged drying were subsequently repeated. All transmission spectra before and after BSA and anti-BSA adsorption were recorded for comparisons.

■ AUTHOR INFORMATION

Corresponding Authors

*E-mail: kllee@gate.sinica.edu.tw (K.-L.L.).
*E-mail: pkwei@sinica.edu.tw (P.-K.W.).

ORCID ⊙

Xu Shi: 0000-0002-6353-5470
Kosei Ueno: 0000-0002-4882-7854
Hiroaki Misawa: 0000-0003-1070-387X
Pei-Kuen Wei: 0000-0002-3002-0526

Author Contributions

K.-L.L. and P.-K.W. conceived and designed the experiments; K.-L.L., P.-C.T., M.-L.Y., and X.S. performed the experiments; and P.-C.T. and M.-Y.P. did the FDTD calculations. K.-L.L. and P.-C.T. analyzed the data; P.-K.W., K.U., and H.M. contributed materials/analysis tools; and K.-L.L. and P.-K.W. cowrote the paper.

Notes

The authors declare no competing financial interest.

■ REFERENCES

(1) Raether, H. *Surface Plasmons on Smooth and Rough Surfaces and on Gratings*; Springer Tracts in Modern Physics; Springer, 1988; Vol. 111.

(2) Homola, J.; Yee, S. S.; Gauglitz, G. Surface plasmon resonance sensors: review. *Sens. Actuators, B* **1999**, *54*, 3−15.

(3) Maier, S. A. *Plasmonics: Fundamentals and Applications*; Springer-Verlag: New York, 2007.

(4) Homola, J. Surface plasmon resonance sensors for detection of chemical and biological species. *Chem. Rev.* **2008**, *108*, 462−493.

(5) Anker, J. N.; et al. Biosensing with plasmonic nanosensors. *Nat. Mater.* **2008**, *7*, 442−453.

(6) Brolo, A. G.; Gordon, R.; Leathem, B.; Kavanagh, K. L. Surface plasmon sensor based on the enhanced light transmission through arrays of nanoholes in gold films. *Langmuir* **2004**, *20*, 4813−4815.

(7) Henzie, J.; Lee, M. H.; Odom, T. W. Multiscale patterning of plasmonic metamaterials. *Nat. Nanotechnol.* **2007**, *2*, 549−554.

(8) Gordon, R.; Sinton, D.; Kavanagh, K. L.; Brolo, A. G. A new generation of sensors based on extraordinary optical transmission. *Acc. Chem. Res.* **2008**, *41*, 1049−1057.

(9) Yanik, A. A.; et al. Seeing protein monolayers with naked eye through plasmonic Fano resonances. *Proc. Natl. Acad. Sci. U.S.A* **2011**, *108*, 11784−11789.

(10) Lee, K.-L.; Lee, C.-W.; Wang, W.-S.; Wei, P.-K. Sensitive biosensor array using surface plasmon resonance on metallic nanoslits. *J. Biomed. Opt.* **2007**, *12*, 044023.

(11) Shen, Y.; et al. Plasmonic gold mushroom arrays with refractive index sensing figures of merit approaching the theoretical limit. *Nat. Commun.* **2013**, *4*, 2381.

(12) Norek, M.; Włodarski, M.; Matysik, P. UV plasmonic-based sensing properties of aluminum nanoconcave arrays. *Curr. Appl. Phys.* **2014**, *14*, 1514−1520.

(13) Skinner, J. L.; Hunter, L. L.; Talin, A. A.; Provine, J.; Horsley, D. A. Large-area subwavelength aperture arrays fabricated using nano-imprint lithography. *IEEE Trans. Nanotechnol.* **2008**, *7*, 527−531.

(14) Canalejas-Tejero, V.; Herranz, S.; Bellingham, A.; Moreno-Bondi, M. C.; Barrios, C. A. Passivated aluminum nanohole arrays for label-free biosensing applications. *ACS Appl. Mater. Interfaces* **2014**, *6*, 1005−1010.

(15) Barrios, C. A.; et al. Aluminum nanohole arrays fabricated on polycarbonate for compact disc-based label-free optical biosensing. *Plasmonics* **2014**, *9*, 645−649.

(16) Chan, G. H.; Zhao, J.; Schatz, G. C.; Van Duyne, R. P. Localized surface plasmon resonance spectroscopy of triangular aluminum nanoparticles. *J. Phys. Chem. C* **2008**, *112*, 13958−13963.

(17) Lee, K.-L.; Hsu, H.-Y.; You, M.-L.; Chang, C.-C.; Pan, M.-Y.; Shi, X.; Ueno, K.; Misawa, H.; Wei, P.-K. Highly sensitive aluminum-based biosensors using tailorable Fano resonances in capped nanostructures. *Sci. Rep.* **2017**, *7*, 44104.

(18) Canalejas-Tejero, V.; Herranz, S.; Bellingham, A.; Moreno-Bondi, M. C.; Barrios, C. A. Passivated aluminum nanohole arrays for label-free biosensing applications. *ACS Appl. Mater. Interfaces* **2014**, *6*, 1005−1010.

(19) Jung, L. S.; Campbell, C. T.; Chinowsky, T. M.; Mar, M. N.; Yee, S. S. Quantitative interpretation of the response of surface plasmon resonance sensors to adsorbed films. *Langmuir* **1998**, *14*, 5636−5648.

(20) Stewart, M. E.; et al. Quantitative multispectral biosensing and 1D imaging using quasi-3D plasmonic crystals. *Proc. Natl. Acad. Sci. U.S.A.* **2006**, *103*, 17143−17148.

(21) Das, M.; Hohertz, D.; Nirwan, R.; Brolo, A. G.; Kavanagh, K. L.; Gordon, R. Improved Performance of Nanohole Surface Plasmon Resonance Sensors by the Integrated Response Method. *IEEE Photonics J.* **2011**, *3*, 441−449.

(22) Lee, K.-L.; Wei, P.-K. Enhancing surface plasmon detection using ultrasmall nanoslits and a multispectral integration method. *Small* **2010**, *6*, 1900−1907.

(23) Lee, K.-L.; et al. Improving surface plasmon detection in gold nanostructures using a multi-polarization spectral integration method. *Adv. Mater* **2012**, *24*, OP253−OP259.

(24) Im, H.; et al. Template-stripped smooth Ag nanohole arrays with silica shells for surface plasmon resonance biosensing. *ACS Nano* **2011**, *5*, 6244−6253.

(25) Nagpal, P.; Lindquist, N. C.; Oh, S.-H.; Norris, D. J. Ultrasmooth patterned metals for plasmonics and metamaterials. *Science* **2009**, *325*, 594−597.

(26) Hegner, M.; Wagner, P.; Semenza, G. Ultralarge atomically flat template-stripped Au surfaces for scanning probe microscopy. *Surf. Sci.* **1993**, *291*, 39−46.

(27) Lee, K.-L.; et al. Enhancing surface plasmon detection using template-stripped gold nanoslit arrays on plastic films. *ACS Nano* **2012**, *6*, 2931−2939.

(28) Fano, U. The theory of anomalous diffraction gratings and of quasi-stationary waves on metallic surfaces (Sommerfeld's waves). *J. Opt. Soc. Am.* **1941**, *31*, 213−222.

(29) Miroshnichenko, A. E.; Flach, S.; Kivshar, Y. S. Fano resonances in nanoscale structures. *Rev. Mod. Phys.* **2010**, *82*, 2257−2298.

(30) Luk'yanchuk, B.; et al. The Fano resonance in plasmonic nanostructures and metamaterials. *Nat. Mater.* **2010**, *9*, 707−715.

(31) Lee, K.-L.; Huang, J.-B.; Chang, J.-W.; Wu, S.-H.; Wei, P.-K. Ultrasensitive biosensors using enhanced Fano resonances in capped gold nanoslit arrays. *Sci. Rep.* **2015**, *5*, 8547.

(32) Lee, K.-L.; Chang, C.-C.; You, M.-L.; Pan, M.-Y.; Wei, P.-K. Enhancing the surface sensitivity of metallic nanostructures using oblique-angle-induced Fano resonances. *Sci. Rep.* **2016**, *6*, 33126.

(33) Gao, H.; et al. Using the angle-dependent resonances of molded plasmonic crystals to improve the sensitivities of biosensors. *Nano Lett.* **2010**, *10*, 2549−2554.

(34) Manera, M. G.; et al. Enhanced magneto-optical SPR platform for amine sensing based on Zn porphyrin dimers. *Sens. Actuators, B* **2013**, *182*, 232−238.

(35) Manera, M. G.; Ferreiro-Vila, E.; Garcia-Martin, J. M.; Garcia-Martin, A.; Rella, R. Enhanced antibody recognition with a magneto-optic surface plasmon resonance (MO-SPR) sensor. *Biosens. Bioelectron.* **2014**, *58*, 114.

(36) Maccaferri, N.; et al. Ultrasensitive and label-free molecular-level detection enabled by light phase control in magnetoplasmonic nanoantennas. *Nat. Commun.* **2015**, *6*, 6150.

(37) Caballero, B.; García-Martín, A.; Cuevas, J. C. Hybrid magnetoplasmonic crystals boost the performance of nanohole arrays as plasmonic sensors. *ACS Photonics* **2016**, *3*, 203−208.

(38) Lahav, A.; Auslender, M.; Abdulhalim, I. Sensitivity enhancement of guided-wave surface-plasmon resonance sensors. *Opt. Lett.* **2008**, *33*, 2539−2541.

(39) Anker, J. N.; et al. Biosensing with plasmonic nanosensors. *Nat. Mater.* **2008**, *7*, 442−453.

(40) Liu, N.; et al. Planar metamaterial analogue of electromagnetically induced transparency for plasmonic sensing. *Nano Lett.* **2010**, *10*, 1103−1107.

(41) Lahav, A.; Auslender, M.; Abdulhalim, I. Sensitivity enhancement of guided-wave surface-plasmon resonance sensors. *Opt. Lett.* **2008**, *33*, 2539−2541.

(42) Gordon, R. Light in a subwavelength slit in a metal: propagation and reflection. *Phys. Rev. B: Condens. Matter Mater. Phys.* **2006**, *73*, 153405.

(43) Lee, K.-L.; Wu, S.-H.; Lee, C.-W.; Wei, P.-K. Sensitive biosensors using Fano resonance in single gold nanoslit with periodic grooves. *Opt. Express* **2011**, *19*, 24530−24539.

(44) Chang, S.-H.; Gray, S. K.; Schatz, G. C. Surface plasmon generation and light transmission by isolated nanoholes and arrays of nanoholes in thin metal films. *Opt. Express* **2005**, *13*, 3150−3165.

(45) Malic, L.; Morton, K.; Clime, L.; Veres, T. All-thermoplastic nanoplasmonic microfluidic device for transmission SPR biosensing. *Lab Chip* **2013**, *13*, 798−810.

(46) Brolo, A. G. Plasmonics for future biosensors. *Nat. Photonics* **2012**, *6*, 709−713.

(47) Shivatare, S. S.; et al. Modular synthesis of N-glycans and arrays for the hetero-ligand binding analysis of HIV antibodies. *Nat. Chem.* **2016**, *8*, 338−346.

(48) Lee, K.-L.; Wu, T.-Y.; Hsu, H.-Y.; Yang, S.-Y.; Wei, P.-K. Low-cost and rapid fabrication of metallic nanostructures for sensitive biosensors using hot-embossing and dielectric-heating nanoimprint methods. *Sensors* **2017**, *17*, 1548.